



# Improved simulation of regional CO<sub>2</sub> surface concentrations using GEOS-Chem and fluxes from VEGAS

Z. H. Chen<sup>1</sup>, J. Zhu<sup>2</sup>, and N. Zeng<sup>3</sup>

<sup>1</sup>International Center for Climate and Environment Science, Institute of Atmospheric Physics, Chinese Academy of Sciences, Beijing 100029, China

<sup>2</sup>State Key Laboratory of Atmospheric Boundary Layer Physics and Atmospheric Chemistry (LAPC), Institute of Atmospheric Physics, Chinese Academy of Sciences, Beijing 100029, China

<sup>3</sup>Department of Meteorology and Earth System Science Interdisciplinary Center, University of Maryland, College Park, Maryland 20742-2425, USA

Correspondence to: Z. H. Chen (czh@mail.iap.ac.cn)

Received: 11 September 2012 – Published in Atmos. Chem. Phys. Discuss.: 22 January 2013

Revised: 12 June 2013 – Accepted: 2 July 2013 – Published: 7 August 2013

**Abstract.** CO<sub>2</sub> measurements have been combined with simulated CO<sub>2</sub> distributions from a transport model in order to produce the optimal estimates of CO<sub>2</sub> surface fluxes in inverse modeling. However, one persistent problem in using model–observation comparisons for this goal relates to the issue of compatibility. Observations at a single station reflect all underlying processes of various scales. These processes usually cannot be fully resolved by model simulations at the grid points nearest the station due to lack of spatial or temporal resolution or missing processes in the model. In this study the stations in one region were grouped based on the amplitude and phase of the seasonal cycle at each station. The regionally averaged CO<sub>2</sub> at all stations in one region represents the regional CO<sub>2</sub> concentration of this region. The regional CO<sub>2</sub> concentrations from model simulations and observations were used to evaluate the regional model results. The difference of the regional CO<sub>2</sub> concentration between observation and modeled results reflects the uncertainty of the large-scale flux in the region where the grouped stations are. We compared the regional CO<sub>2</sub> concentrations between model results with biospheric fluxes from the Carnegie-Ames-Stanford Approach (CASA) and VEgetation-Global-Atmosphere-Soil (VEGAS) models, and used observations from GLOBALVIEW-CO<sub>2</sub> to evaluate the regional model results. The results show the largest difference of the regionally averaged values between simulations with fluxes from VEGAS and observations is less than 5 ppm for North American boreal, North American temperate, Eurasian boreal, Eurasian

temperate and Europe, which is smaller than the largest difference between CASA simulations and observations (more than 5 ppm). There is still a large difference between two model results and observations for the regional CO<sub>2</sub> concentration in the North Atlantic, Indian Ocean, and South Pacific tropics. The regionally averaged CO<sub>2</sub> concentrations will be helpful for comparing CO<sub>2</sub> concentrations from modeled results and observations and evaluating regional surface fluxes from different methods.

## 1 Introduction

An improved understanding of the carbon sources and sinks at a regional scale globally is essential to predict the future rate of atmospheric CO<sub>2</sub> increases and to plan an international CO<sub>2</sub> management strategy (Ciais et al., 2010). But these fluxes remain quantitatively uncertain. The full range of results in past studies spans budgets with northern terrestrial uptake of 0.5 to 4 PgC yr<sup>-1</sup>, and tropical terrestrial emissions of –1 to 4 PgC yr<sup>-1</sup> (Stephens et al., 2007; Peylin et al., 2002; Gurney, 2004). Some studies show increasing sinks in tropical forest plots (Baker et al., 2004). Rising temperatures may already decrease the efficiency of terrestrial carbon uptake in the Northern Hemisphere (Piao et al., 2008), while larger net sinks were found over northern and southern continents than the results of the TransCom-3 study for 1992–1996 (Feng et al., 2011).

Where and when atmospheric CO<sub>2</sub> is absorbed by land ecosystems and oceans is a major issue for the global carbon cycle. Optimized estimates of surface sources and sinks have been produced in different ways. One is a top-down way. For example, CO<sub>2</sub> in the atmosphere is affected by surface fluxes. Information about regional carbon sources and sinks can be derived from variations in observed atmospheric CO<sub>2</sub> concentrations via inverse modeling with atmospheric tracer transport models (Gurney et al., 2002). Another is a bottom-up way. For example, the land-atmosphere fluxes can be simulated by different dynamic global vegetation models (DGVMs) (Sitch et al., 2008). Terrestrial carbon cycle model VEGAS (Vegetation-Global-Atmosphere-Soil) is one of the DGVMs that was developed to simulate the net land-atmosphere fluxes and has been described by Zeng (2003). The land-atmosphere flux simulated by VEGAS agrees well with the CO<sub>2</sub> growth rate observed at Mauna Loa both in terms of interannual amplitude and phase (Zeng et al., 2005).

The GEOS-Chem atmospheric transport model has been widely used in the assimilation of CO<sub>2</sub> and inverse of CO<sub>2</sub> flux. It has been used to evaluate the influence of reduced carbon emissions on the distribution of atmospheric CO<sub>2</sub> and described in early studies (Suntharalingam, 2004, 2005). The land-atmosphere fluxes in GEOS-Chem include monthly biomass burning CO<sub>2</sub> emissions, annual inventory of biofuel burning 3-hourly net ecosystem productivity (NEP) for 2000 (Olsen, 2004), and annual climatology based on TransCom CO<sub>2</sub> inversion results in Nassar et al. (2010). The differences between CO<sub>2</sub> model simulation using surface fluxes and observations have been used to improve our understanding of the global surface fluxes. There were different methods to compare CO<sub>2</sub> model results and observations in earlier studies. The mean annual meridional/longitudinal gradient observation is compared with model values (Bousquet et al., 1999; Kaminski et al., 1998). Latitudinal distribution of the sources and sinks of CO<sub>2</sub> from the concentration gradient has been discussed (Tans et al., 1989, 1990). The air samples in flasks were grouped into latitude bands to aid determination of the sources and sinks (Tans et al., 1989). Previous studies have adjusted the CO<sub>2</sub> surface flux via minimizing the distance between the modeled/optimized values and the observational data at each station (Enting, 2002; Peylin et al., 2002; Bousquet, 2000; Baker et al., 2006; Gurney et al., 2002; Rödenbeck et al., 2006).

However, one persistent problem in using model-observation comparisons for this goal relates to the issue of compatibility. Observations at a single station reflect all underlying processes of all scales. These processes cannot be fully resolved by model simulations at the grid points nearest to the station due to the lack of spatial or temporal resolution or missing processes in the model. In this article we propose a new technique to evaluate the regional surface fluxes by comparing the regional CO<sub>2</sub> concentration from model simulations with observations, rather than the difference at every single observational station. Several stations in

one region were grouped according to the regional temporal characteristics of the seasonal cycle, which have been derived from a new atmospheric CO<sub>2</sub> observation data set from GLOBALVIEW-CO<sub>2</sub> 2010. The averaged concentration of CO<sub>2</sub> at all stations in one region represents the regional CO<sub>2</sub> concentration in this region.

To validate the usefulness of the new evaluation method about regionally averaged CO<sub>2</sub> concentrations, we compared two simulations using two different emission inventories with observations. One emission inventory is the original surface fluxes in GEOS-Chem, including the NEP from Carnegie-Ames-Stanford Approach (CASA). Another new emission inventory, including the land-atmosphere fluxes from VEGAS, was selected to reproduce CO<sub>2</sub> concentrations in this study. The land-atmosphere fluxes from VEGAS were used in the GEOS-Chem model, replacing all the current inventories except anthropogenic emissions and ocean fluxes.

The outline of this paper is as follows: Sect. 2 introduces the data. Section 3 describes the grouping of observation stations in one region and demonstrates the temporal and spatial variability in CO<sub>2</sub>. Section 4 presents the differences between the modeled regional CO<sub>2</sub> concentrations with fluxes from CASA and the modeled results with fluxes from VEGAS. We present conclusions in Sect. 5.

## 2 Data

### 2.1 GLOBALVIEW CO<sub>2</sub> data

GLOBALVIEW-CO<sub>2</sub> (GLOBALVIEW-CO<sub>2</sub>, 2010) is a product of the Cooperative Atmospheric Data Integration Project. The project is coordinated and maintained by the Carbon Cycle Greenhouse Gases Group of the National Oceanic and Atmospheric Administration, Earth System Research Laboratory (NOAA ESRL). Gaps in the data are filled by extrapolation from marine boundary layer measurements. Flask samples of whole air enable highly accurate and precise measurements of atmospheric CO<sub>2</sub> concentrations (Conway et al., 1994). This data product includes more than 300 extended records derived from observations made by 22 laboratories from 15 countries in the period 1 January 1979 to 1 January 2010. Data in the files with a sea qualifier that contain a statistical summary of the average seasonal pattern by month were used to analyze the seasonal cycle of the observation stations. Data in the files with an ext qualifier that contain synchronized smoothed values were compared with model results. Where there are several measurements at different altitudes for the same station we only use the lowest in altitude. This gives a total of 108 measurements that were used.

## 2.2 Modeling the land carbon fluxes

The net ecosystem exchange (NEE) is simulated by DGVMs and equals the heterotrophic respiration (RH) subtracted from the net primary productivity (NPP). Simulated land–atmosphere fluxes are between  $-1.52 \text{ PgC yr}^{-1}$  (Lund-Postdam-Jena (LPJ) model) and  $-2.75 \text{ PgC yr}^{-1}$  (Sheffield-DGVM (SHE) model) for the 1990s. The DGVMs simulate a greater land carbon uptake, which is in agreement with IPCC estimates (Sitch et al., 2008). The land fluxes are defined as the sum of photosynthesis, ecosystem respiration and biomass burning. The terrestrial carbon model VEGAS is described in Zeng (2003). It was run at  $2.5^\circ \times 2.5^\circ$  resolution and forced by precipitation and temperature, the seasonal climatologies of radiation, humidity, and wind speed. The driving data of precipitation for VEGAS come from a combination of the Climate Research Unit (CRU; New et al., 1999; Mitchell and Jones, 2005) data set for the period of 1901–1979 and the Xie and Arkin (1996) data set of 1980–2006 (which has been adjusted with the 1981–2000 climatology of CRU data set). The surface air temperature driving data use the data set from NASA's Goddard Institute for Space Studies (GISS) by Hansen et al. (1999), adjusted by CRU climatology of 1961–1990. A fire module includes the effects of moisture availability, fuel loading, and plant functional type dependent resistance. Unique features of VEGAS include a vegetation height dependent maximum canopy, which introduces a decadal timescale that can be important for feedback into climate variability and a decreasing temperature dependence of respiration from fast to slow soil pools. Specially, two lower soil pools have weaker temperature dependence of decomposition due to physical protection underground in VEGAS (Q10 value of 2.2 for the fast pool, 1.35 for the intermediate pool, and 1.1 for the slow pool). The monthly land–atmosphere fluxes simulated by VEGAS are regridded offline to the GEOS grids ( $2^\circ \times 2.5^\circ$ ) in this study, which is equal to the magnitude of NEE. The seasonal cycle of land–atmosphere fluxes from VEGAS is shown in Fig. 1. A positive flux indicates a flux of CO<sub>2</sub> from the land to atmosphere and negative is uptake by the land.

Monthly mean NEP fluxes for 2000 from CASA are constructed from gross primary production (GPP) and ecosystem respiration (Re) (Olsen, 2004). Inputs to CASA included a 1990 monthly normalized difference vegetation index (NDVI) product derived from the NOAA/NASA Pathfinder data set, surface solar insolation (Bishop and Rossow, 1991), mean temperature and precipitation from the period 1950 to 1980 (Shea, 1986), soil texture (Zobler, 1986), and a land cover classification based on NDVI (DeFries and Townshend, 1994). The response of heterotrophic respiration to surface air temperature is described by using a Q10 function of 1.5 (Raich and Potter, 1995). The net global contribution from CASA is set to  $0 \text{ PgC yr}^{-1}$  in order to represent terrestrial fluxes with no anthropogenic interference. The seasonal cycle of NEP from CASA is shown in Fig. 1.

Anthropogenic interferences such as biomass burning were specified as  $2.96 \text{ PgC yr}^{-1}$  in GEOS-Chem. To account for the total annual sum of biospheric uptake and emission of CO<sub>2</sub>, the residual annual terrestrial exchange of inverse results from TransCom, a global total of  $-5.29 \text{ PgC yr}^{-1}$ , was included in the land–atmosphere fluxes (Nassar et al., 2010). The seasonal cycle of total land–atmosphere fluxes used in GEOS-Chem is shown in Fig. 1.

The original CO<sub>2</sub> fluxes used in this study include  $7.8 \text{ PgC}$  (anthropogenic emissions),  $-1.4 \text{ PgC}$  (net ocean–atmosphere fluxes), and  $-2.3 \text{ PgC}$  (net land–atmosphere fluxes) for 2006. The original global annual net CO<sub>2</sub> flux for 2006 is  $4.1 \text{ PgC}$ . The new CO<sub>2</sub> fluxes used in this study include  $7.8 \text{ PgC}$  (anthropogenic emissions),  $-1.4 \text{ PgC}$  (net ocean–atmosphere fluxes), and  $-1.9 \text{ PgC}$  (net land–atmosphere fluxes) for 2006. The new global annual net CO<sub>2</sub> flux for 2006 is  $4.5 \text{ PgC}$ . There are also little differences between the total fluxes from other inversion results. JENA S99V3.2 data ( $3.78 \text{ PgC}$ ) are available from <http://www.bgc-jena.mpg.de/~christian.roedenbeck/download-CO2/>; LSCE V1.0 ( $3.43 \text{ PgC}$ ) (Chevallier et al., 2010) is available from <http://www.carboscope.eu/>; Carbon Tracker –2009 ( $4.15 \text{ PgC}$ ) is available from <http://www.esrl.noaa.gov/gmd/ccgg/carbontracker/>; and two inversion results ( $4.1 \text{ PgC}$ ,  $4.7 \text{ PgC}$ ) are from Feng et al. (2011) and Nassar et al. (2011).

The land–atmosphere flux from VEGAS in January is  $270 \text{ TgC}$  less than that from CASA. These differences are distributed over tropical land regions as shown in Fig. 2. The fluxes from VEGAS are smaller than the original land–atmosphere flux in GEOS-Chem, especially from June to August (about  $460 \text{ TgC}$ ,  $770 \text{ TgC}$ , and  $180 \text{ TgC}$ , respectively). The differences between the flux from VEGAS and that from CASA in July are distributed over the regions of Asia, temperate North America, and tropical South America (Fig. 3), which reaches about  $500 \text{ TgC}$  in total.

## 3 Regionally averaged CO<sub>2</sub> observations

### 3.1 Determining groups of observational stations

We grouped several observation stations in one region based on the seasonal cycle at each station in our study. The stations in one region were grouped based on the amplitude and phase of the seasonal cycles at each station. The average of CO<sub>2</sub> at all stations in one region represents the regional CO<sub>2</sub> concentrations. The amplitude and phase of the seasonal cycle at each station in one group are similar, while the average amplitude and phase of the seasonal cycle for each group are different from that of other groups. There are 36 stations on the land and 72 stations on the ocean (see Table A1). These stations were classified into 26 groups. A map of all grouped stations is shown in Fig. 4.

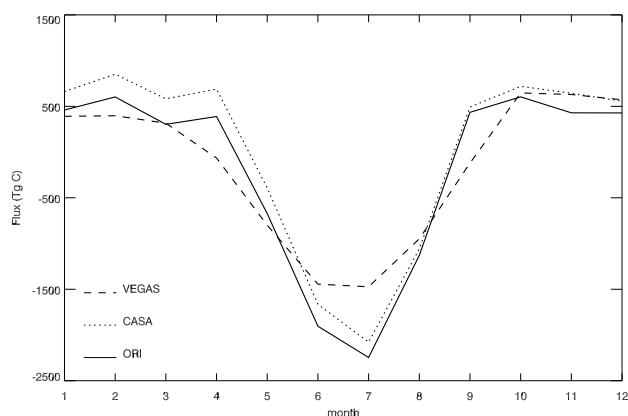


**Fig. 1.** Monthly terrestrial fluxes from dynamic global vegetation models (CASA and VEGAS) and original land–atmosphere fluxes (ORI, including fluxes from CASA, biofuel burning, biomass burning and residual annual biospheric flux) in GEOS-Chem in 2006.

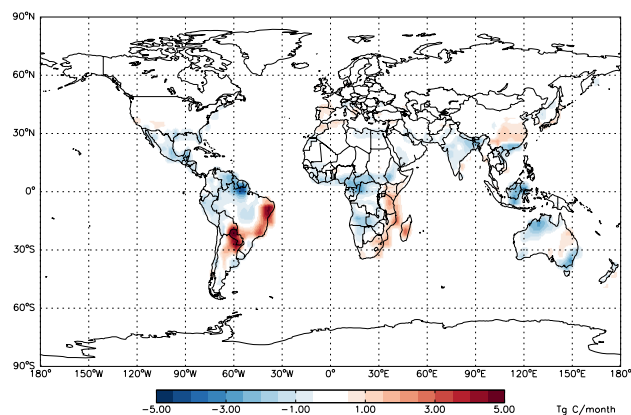


**Fig. 2.** Spatial distribution of difference between terrestrial exchange from CASA and fluxes from VEGAS in January 2006 (positive values denote the fluxes from VEGAS are greater than the fluxes from CASA).

All stations on the land show similar seasonal cycles. The concentration of CO<sub>2</sub> decreases during summer and autumn and increases during spring and winter. The difference between minimum and maximum values is greater than 6 ppm for most stations on the land. We cannot split the land based on the seasonal cycles at stations on the land because the phase of seasonal cycles at all stations on the land is similar; for example, CO<sub>2</sub> at all stations on the land decreases in autumn and increases in spring. The land was divided into 11 regions based on the TransCom land regions (shown in Fig. 4). The land region north of 40° N in North America is called boreal North America (L1), and the region south of 40° N in North America is called temperate North America (L2). The region north of 5° S in South America is called South America tropical (L3), and the region south of 5° S in South America is called South America temperate (L4). The

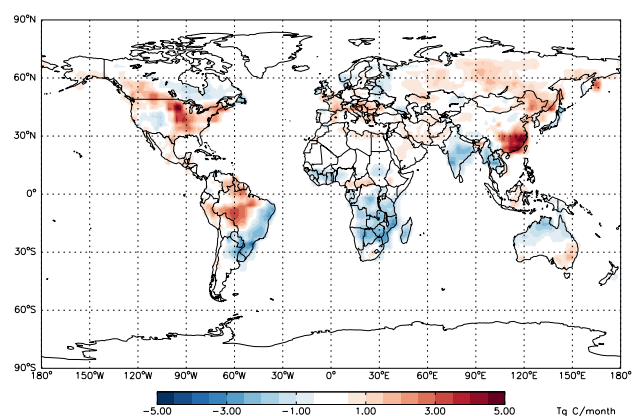


**Fig. 3.** Difference of spatial distribution between terrestrial exchange from CASA and fluxes from VEGAS in July 2006.

other seven land regions are northern Africa (L5), southern Africa (L6), Eurasian boreal (L7), Eurasian temperate (L8), tropical Asia (L9), Australia (L10), and Europe (L11). The stations in each land region were grouped. The magnitude of the amplitude of the seasonal cycles at different stations in one land region may be different. To represent the regional CO<sub>2</sub> concentration for the land regions, the averages of seasonal cycles at more than two stations with similar amplitudes were required in one land region. There are more than 2 stations with similar amplitudes of seasonal cycles in only 5 land regions (North America, temperate North America, Eurasian boreal, Eurasian temperate, and Europe). Therefore, the regional CO<sub>2</sub> concentrations of these 5 land regions were used to evaluate the observation–model differences of CO<sub>2</sub>.

The amplitude and phase of seasonal cycles at stations on the ocean are different. For example, CO<sub>2</sub> decreases in April for one region while in August for another region. The stations on the ocean were grouped based on the amplitude and phase of seasonal cycle. The stations on the ocean were grouped into 15 groups, and the ocean was divided into 15 regions in this study. The 11 ocean basis regions were chosen to approximate circulation features such as gyres and upwelling regions in the TransCom study (Gurney et al., 2002).

### 3.2 Seasonal cycles of stations on the land

The seasonal cycles at all stations in 5 land regions are shown in Fig. 5. The annual mean has been removed. The average minimal value for each region is smaller than −7 ppm (−11.5 ppm for North American boreal (L1), −7.1 ppm for North American temperate (L2), −10 ppm for Eurasian boreal (L7), −8.7 ppm for Eurasian temperate (L8), −8.1 ppm for Europe (L11)). Seasonal cycles of atmospheric CO<sub>2</sub> are caused primarily by the terrestrial biosphere moving from being a net source of carbon to the atmosphere (mainly in winter) to becoming a net sink (mainly in summer), where

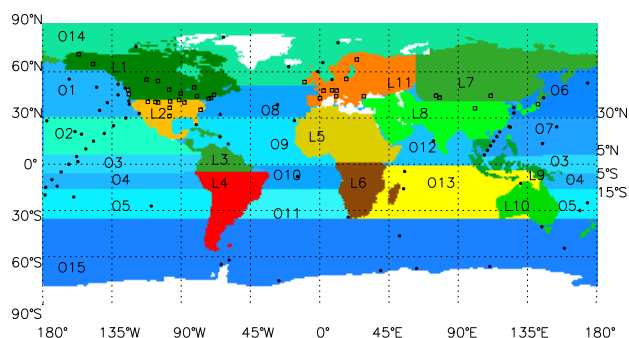


**Fig. 4.** The locations of the observing stations (72 stations on the ocean (closed circle), 36 stations on the land (open square)), and the regions over the globe (15 ocean regions and 11 land regions). The stations in one region were grouped. The ocean was divided into 15 regions, and the stations on the ocean were grouped into 15 groups. The land was divided into 11 regions, and the stations on the land were grouped into 11 groups. L1: North American boreal, L2: North American temperate, L3: South American tropical, L4: South American temperate, L5: northern Africa, L6: southern Africa, L7: Eurasian boreal, L8: Eurasian temperate, L9: tropical Asia, L10: Australia, L11: Europe, O1: northeast Pacific, O2: northeast Pacific temperate, O3: Pacific tropics, O4: South Pacific tropics, O5: South Pacific temperate, O6: northwest Pacific, O7: northwest Pacific temperate, O8: North Atlantic, O9: North Atlantic temperate, O10: Atlantic tropics, O11: South Atlantic temperate, O12: Indian tropical, O13: South Indian temperate, O14: northern ocean, O15: Southern Ocean.

net carbon uptake or release is determined by the balance between photosynthesis and respiration, which vary in response to temperature and precipitation anomalies. Studies have shown the seasonal cycle of atmospheric CO<sub>2</sub> in the Northern Hemisphere (NH) is in phase with the ecosystems (e.g., Randerson et al., 1997). The geographic domain from which surface fluxes influence the measured seasonal variation in gas concentration can be assessed through a footprint analysis (Randerson et al., 1997). The fluxes in this domain could be adjusted according to the differences between the modeled regional CO<sub>2</sub> concentrations and observations. The difference in seasonal amplitude of all groups in the NH can be an important constraint for further improving our understanding of the surface fluxes in the NH.

### 3.3 Seasonal cycles of stations on the ocean

The ocean was divided into 15 regions based on the seasonal cycles of CO<sub>2</sub>, including Pacific Ocean region (O1–O7), Atlantic regions (O8–O11), Indian regions (O12–O13), northern ocean (O14), and Southern Ocean (O15) in this study.

The stations within the Pacific Ocean north of 5° S were classified into 5 different groups (O1, O2, O3, O6 and O7), and the stations within the Atlantic Ocean were classified into 2 groups (O8 and O9). Though the seasonal cycles of the ocean regions north of 5° S were similar to that of the land groups in Northern Hemisphere, there are different

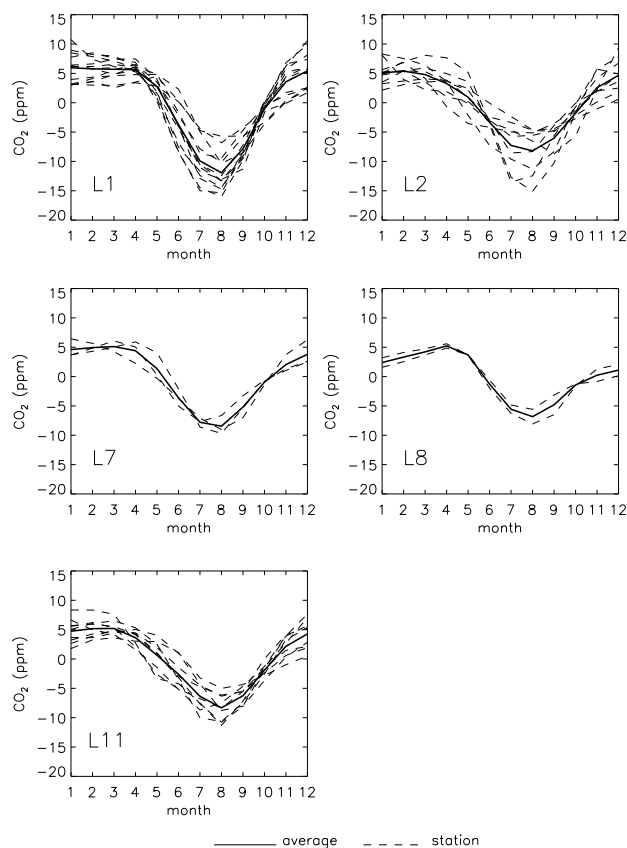


**Fig. 5.** Seasonal cycles of observational stations in 5 land regions where there are more than 2 stations (L1: boreal North America, L2: temperate North America, L7: Eurasian boreal, L8: Eurasian temperate, L11: Europe). 5 regions are shown in Fig. 4. Broken line denotes the seasonal values for all stations in one region; solid line denotes the grouped average value of each region. The stations within the region North American boreal (L1) are labeled with “L1” in the “group” columns of Table A1. The way to find the stations in other regions is similar.

amplitudes (as shown in Fig. 6). The amplitudes of groups O1 and O6 are larger than 10 ppm, and the amplitudes of O2 and O7 are much less than that of other northern regions, while the amplitude of group O3 is much less than 6 ppm. The amplitude of group O9 is less than that of group O8. The amplitude is less in the Southern Hemisphere (SH), since the Southern Hemisphere has less mid-latitude vegetation to absorb and release CO<sub>2</sub> seasonally (Randerson et al., 1997).

The South Pacific region between 5° S and 35° S was divided into two subregions (O4 and O5) according to the different seasonal cycles of CO<sub>2</sub> measured at stations in these regions. Though the amplitude is smaller than 1.4 ppm, the CO<sub>2</sub> seasonal cycle of the groups is clear in these regions. Generally there is an increase period and a decrease period for one seasonal cycle. While CO<sub>2</sub> increases from April to June and from October to December for the South Pacific tropics (O4), CO<sub>2</sub> decreases from January to April and from August to October for the South Pacific temperate (O5).

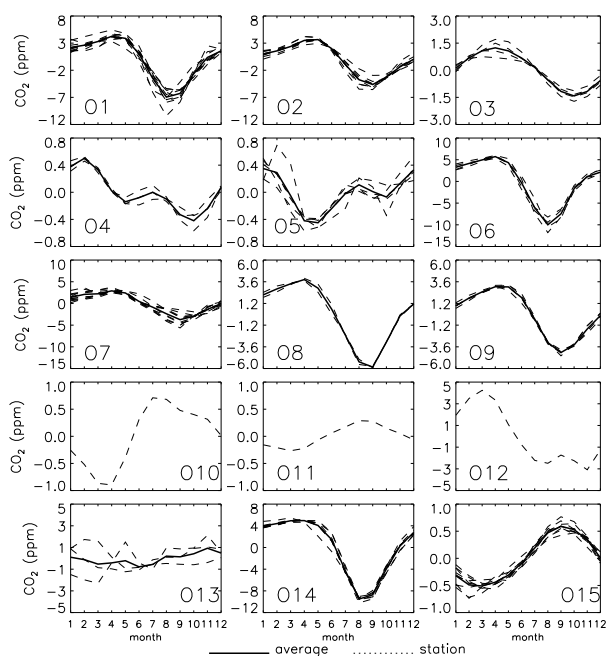


**Fig. 6.** Seasonal cycles of observational stations of 15 ocean groups in ocean regions (15 regions are shown in Fig. 4). Broken line denotes the seasonal values for all stations in one region; solid line denotes the regional averaged value of each region. The stations within the region northeast Pacific (O1) are labeled with “O1” in the “group” columns of Table A1. The way to find the stations in other regions is similar.

The seasonal cycles are more complicated in the Indian Ocean north of 35° S. They were classified into two groups with different seasonal cycles (O12 and O13). The average seasonal cycles of these two regions are different from other ocean regions. The North Indian Ocean (O12) shows a consistent decrease from February to November. The concentrations of stations within the South Indian Ocean (O13) range from −1.5 ppm to 1.5 ppm during the first half year and show an increase (about 1 ppm) in the second half year. The South Atlantic was divided into 2 regions (O10 and O11) with different amplitudes. The minimum and maximum values are −0.9 ppm and 0.7 ppm for the Atlantic tropics (O10), while they are −0.3 ppm and 0.3 ppm for the South Atlantic temperate (O11).

The concentrations of CO<sub>2</sub> at stations within the ocean south of 5° S are mainly influenced by the oceanic sources and sinks, and the amplitudes of seasonal cycles are not more than 2 ppm (O4, O5, O10, O11 and O15), which is much smaller than that of the NH. It is evident that the seasonal anomalies of CO<sub>2</sub> are positive in NH winter (January) and negative in NH summer (August). Inversely, the seasonal variations are positive in the southern hemispheric winter (August) and negative in the southern hemispheric summer (January) south of 35° S (Fig. 6). Seasonal signals observed in all subtropical regions of the NH and SH show that the CO<sub>2</sub> concentration decreases southward in summer and vice

versa in winter (Metzl et al., 2006). An increase of the seasonal cycle for Southern Ocean occurs in September, while the seasonal anomalies of CO<sub>2</sub> in the Northern Hemisphere are negative at the same time. The two seasonal cycles of the Southern Ocean (O15) and the Northern Hemisphere are out of phase. Northern Hemisphere terrestrial ecosystems contribute substantially to the seasonal cycle at many stations in the Southern Hemisphere. Because of lags in transport and nonoverlapping growing seasons, some components from the northern and southern hemispheres are out of phase with one another. Thus, an increase in seasonal cycle of NEP fluxes from terrestrial uptake in the Northern Hemisphere could drive a decrease in the amplitude of the seasonal cycle of atmospheric CO<sub>2</sub> at stations in the Southern Hemisphere (Randerson et al., 1997).

#### 4 Simulation results and comparison with observations

We use the GEOS-Chem model (Suntharalingam, 2004, 2005) to describe the relationship between 3-D atmospheric CO<sub>2</sub> concentrations and surface CO<sub>2</sub> fluxes. A detailed description of the original emission inventory is given in Nassar et al. (2010). Our model simulation was initialized with a uniform global distribution of 375 ppm on 1 January 2004 and integrated forward to 1 January 2006 using the original emission inventory. The modeled CO<sub>2</sub> distribution on 1 January 2006 was the initial concentration for two simulations with the original emission inventory (ori) and the new emission inventory (new) from 1 January 2006 to 1 January 2007. Both model simulations were run at a horizontal resolution of 2° latitude × 2.5° longitude. Figures 7 and 9 show differences between the model results with the original inventory and the results with the new inventory during 2006.

##### 4.1 Comparisons of regionally averaged CO<sub>2</sub> concentrations for land regions

The CO<sub>2</sub> seasonal cycles were simulated by the model with original and new emission inventories. The largest difference between the model results and observations for runs with the original emission inventory is 17.5 ppm, about 4.5 % of observation values. The difference for the simulation with the new emission inventory is below 8.4 ppm, about 2.2 %. The largest differences for both simulations appear in region L11, which indicates there may be large uncertainties for these two CO<sub>2</sub> surface fluxes in Europe.

The difference of the regional CO<sub>2</sub> concentration between model results with the new emission inventory and observations is less than 2 ppm for North American boreal (L1) from January to June, which is smaller than 1 % of observations. The difference is about 2 ppm during July, August, and December, which suggests that there are large uncertainties in North America for the new inventories during these periods. The difference between simulations with the

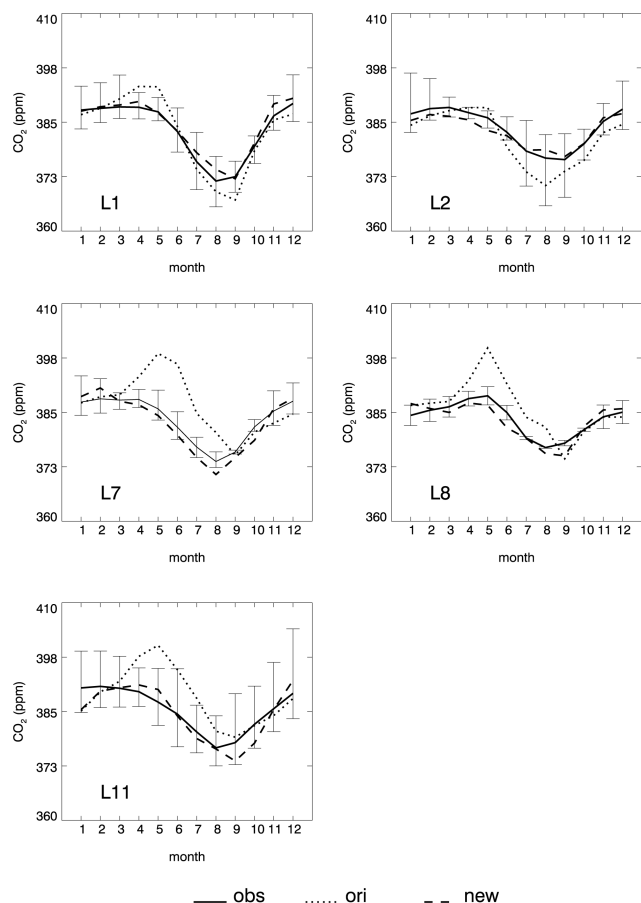


**Fig. 7.** Comparisons of regionally averaged values of CO<sub>2</sub> between model results from GEOS-Chem with the original emission inventory (dotted line) and the new emission inventory (dashed line) and GLOBALVIEW-CO<sub>2</sub> (solid line) for 5 land regions (L1: boreal North America, L2: temperate North America, L7: Eurasian boreal, L8: Eurasian temperate, L11: Europe) in 2006 (5 regions are shown in Fig. 4). The error bar represents the spread of the observations.

original emission inventory and observations reaches 6 ppm from April to May.

The largest difference between the simulation with fluxes from VEGAS and observations is 2.8 ppm for the North American boreal (L1), 2.9 ppm for North American temperate (L2), 3.1 ppm for Eurasian boreal (L7), 3.5 ppm for Eurasian temperate (L8), and 4.3 ppm for Europe (L11), which is smaller than that of CASA (5.8 ppm, 6.3 ppm, 14.5 ppm, 10.9 ppm, 13.1 ppm, respectively). The spread of the regional CO<sub>2</sub> of observations for each region is shown in Fig. 7, which is determined by the concentrations of stations in the region.

The root-mean-square difference (RMSD) of regionally averaged value between model results with fluxes from VEGAS and observation is reduced by 0.24–0.63 ppm for 5 land regions. The RMSD between two simulations and observations for each station ranges from 0 to 2 ppm. As shown in Fig. 8, the largest RMSE between the simulations with fluxes

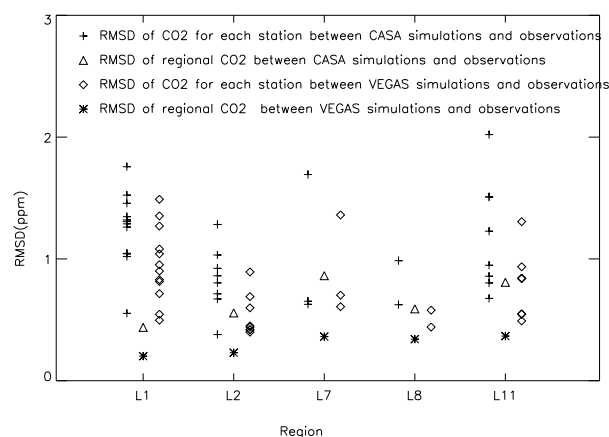


**Fig. 8.** Comparisons of RMSD at each station and regionally averaged values between model results and observations for 5 land regions (L1: boreal North America, L2: temperate North America, L7: Eurasian boreal, L8: Eurasian temperate, L11: Europe) in 2006. Each region is shown in Fig. 4. Triangle (asterisk) denotes RMSD of regionally averaged values between model results using fluxes from CASA (VEGAS) and observations; cross (diamond) denotes RMSD of each station between model results using fluxes from CASA (VEGAS) and observations.

from VEGAS and observations for regional CO<sub>2</sub> concentrations is 0.2 ppm, which is smaller than the value with fluxes from CASA (0.4 ppm).

The new emission inventory can be used as good prior fluxes in the forward model and be adjusted in future inverse models from the above comparisons of 5 land regions.

#### 4.2 Comparisons of regionally averaged CO<sub>2</sub> concentrations for ocean regions

The seasonal cycles of CO<sub>2</sub> concentration at stations on the ocean are also influenced by the change of emission inventories on land. The difference between the simulations with the new inventories and observations ranges from 0.02 ppm to 2 ppm (0.7 ppm to 4 ppm for the old inventories) for the South Pacific temperate (O5) during 2006. It can be deduced that the regional CO<sub>2</sub> concentration of the ocean regions could be improved through the improvement of the land fluxes.

The largest difference (about 8 ppm) for runs with new inventories appears in April 2006 for the Indian tropical region (O12). It is a high value (about 387 ppm) for observations in April 2006, while the simulated result with the new emission inventory is 379 ppm (Fig. 9). Fluxes that contribute to the concentration of this region should be improved for this new emission inventory.

There are differences between both model results and observations from January to April for the South Indian temperate (O13). The peak-to-trough amplitude of the regional CO<sub>2</sub> concentration for this region is no more than 2 ppm in 2006, while the spread of the observed concentrations in this

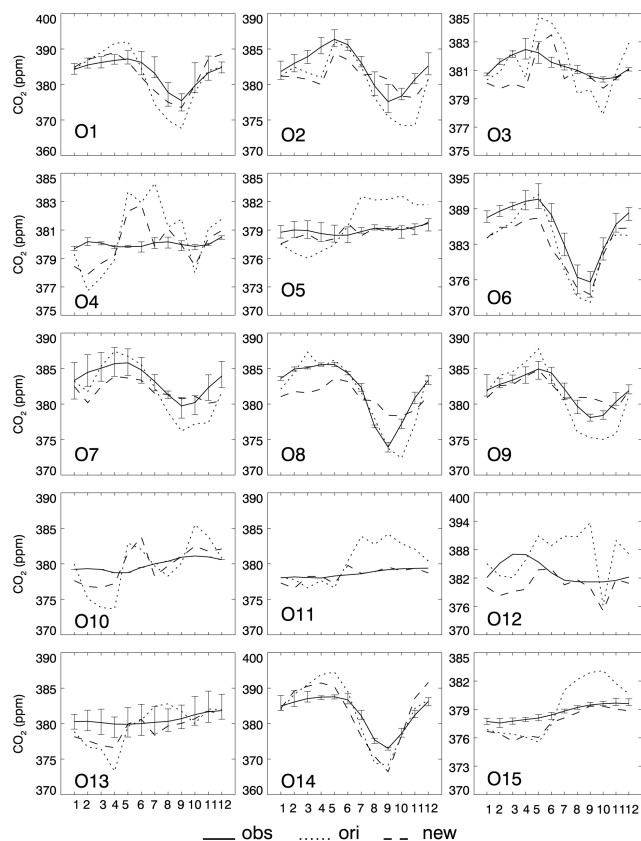


**Fig. 9.** Comparisons of regionally averaged values of CO<sub>2</sub> between model results from GEOS-Chem with the original emission inventory (dotted line) and the new emission inventory (dashed line) and GLOBALVIEW-CO<sub>2</sub> (solid line) for 15 ocean regions in 2006 (15 ocean regions are shown in Fig. 4). The error bar represents the spread of the observations.

region is larger than 2 ppm for all months in 2006. Unfortunately, there are too few observations in the adjacent land regions. Some more observations are very necessary for these regions in the future.

There is still a large positive bias (about 5 ppm) for North Atlantic temperate (O8, O9) from July to September. It is necessary to improve the fluxes in this region or the surrounded land regions. For the South Pacific tropics (O4) and South Pacific temperate (O5), it is difficult to simulate the two increase phases and two decrease phases in the seasonal cycle of observations (Fig. 6). It could be effective for improving the fluxes in the ocean regions to match observations because the seasonal cycle simulated by the land fluxes is characterized by one increase and one decrease phase.

The concentrations of CO<sub>2</sub> at stations on the ocean are influenced by the change of emission inventories on land. As shown in Fig. 10, the RMSD of regionally averaged value between model results using fluxes from VEGAS and observation is less than the results using fluxes from CASA by 0.15–0.53 ppm for northeast Pacific, South Pacific and Southern Ocean (O1, O4, O5, O12, O13 and O15). There is

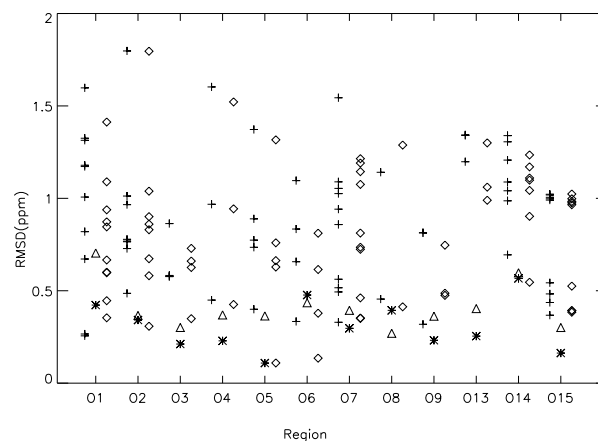


**Fig. 10.** Comparisons of RMSD at each station and regionally averaged values between model results and observations for the ocean regions in 2006. Each region is shown in Fig. 4. Triangle (asterisk) denotes RMSD of regionally averaged values between model results using fluxes from CASA (VEGAS) and observations; cross (diamond) denotes RMSD of each station between model results using fluxes from CASA (VEGAS) and observations (see the legend in Fig. 8).

little improvement for North Pacific and northern ocean (O2, O6, and O14). It is convenient to evaluate the regional model results according to the comparisons of regionally averaged values.

## 5 Conclusions

We grouped several observation stations in one region according to the phase and amplitude of seasonal cycles of measured CO<sub>2</sub>. The regionally averaged values contain less small-scale “noise” that models often cannot resolve and are used to evaluate the regional model results. The differences of regionally averaged values between observations and model results reflect the uncertainties of the flux in the region where the grouped stations are.

We compared regionally averaged values between model results with two land-atmosphere flux from CASA (VEGAS) and observations. Results show that the differences between the modeled regionally averaged values of CO<sub>2</sub> concentrations with fluxes from VEGAS and observations have improvements in most regions. There is still large uncertainty in the Atlantic and North Atlantic, Indian Ocean, and South Pacific tropics.

The regional CO<sub>2</sub> surface fluxes can be estimated by different methods. It is very useful for evaluating regional surface fluxes by comparing the CO<sub>2</sub> regionally averaged values from modeled results with observations. The differences of regionally averaged values between observations and model results can be used to estimate the uncertainty of regional fluxes and to optimize the regional fluxes with inverse methods in future work.

Table A1. Stations used in this paper.

Station_name	Abbreviation	Longitude	Latitude	Height (m a.s.l.)	Group
Cold Bay, Alaska	cba_01D0	-162.72	55.2	25	O1
Cape St. James, BC	csj_06D0	-131.02	51.93	89	O1
Estevan Point, BC	esp005_01P2	-126.55	49.38	500	O1
La Jolla, California	ljo_04D0	-117.3	32.9	10	O1
Pacific Ocean	pocn35_01D1	-143	35	10	O1
Pacific Ocean	pocn40_01D1	-138	40	10	O1
Pacific Ocean	pocn45_01D1	-131	45	10	O1
Point Arena, California	pta_01D0	-123.73	38.95	17	O1
Ocean Station P, Canada	stp_12D0	-145	50	7	O1
Trinidad Head, California	thd005_01P2	-124.15	41.05	500	O1
Molokai Island, Hawaii	haa005_01P2	-158.95	21.23	500	O2
Cape Kumukahi, Hawaii	kum_01D0	-154.82	19.52	3	O2
Sand Island, Midway	mid_01D0	-177.38	28.21	4	O2
Pacific Ocean	pocn10_01D1	-152	10	10	O2
Pacific Ocean	pocn15_01D1	-147	15	10	O2
Pacific Ocean	pocn20_01D1	-140	20	10	O2
Pacific Ocean	pocn25_01D1	-134	25	10	O2
Pacific Ocean	pocn30_01D1	-126	30	10	O2
Christmas Island, Kiribati	chr_01D0	-157.17	1.7	3	O3
Pacific Ocean	poc000_01D1	-163		10	O3
Pacific Ocean	pocn05_01D1	-158	5	10	O3
Pacific Ocean	pocs05_01D1	-168	-5	10	O3
Pacific Ocean	pocs10_01D1	-174	-10	10	O4
Pacific Ocean	pocs15_01D1	-178	-15	10	O4
American Samoa	smo_01C0	-170.57	-14.24	42	O4
Easter Island, Chile	eic_01D0	-109.45	-27.15	50	O5
Pacific Ocean	pocs20_01D1	-178.5	-20	10	O5
Pacific Ocean	pocs25_01D1	174	-25	10	O5
Pacific Ocean	pocs30_01D1	169	-30	10	O5
Rarotonga, Cook Islands	rta005_01P2	-159.83	-21.25	500	O5
Cape Ochi-ishi, Japan	coi_20C0	145.5	43.15	100	O6
Gosan, Cheju Island, South Korea	gsn_24D0	126.15	33.28	72	O6
Shemya Island, Alaska	shm_01D0	174.1	52.72	40	O6
Tae-ahn Peninsula, South Korea	tap_01D0	126.13	36.73	20	O6
Mariana Islands, Guam	gmi_01D0	144.78	13.43	2	O7
Hateruma Island, Japan	hat_20C0	123.8	24.05	47	O7
Minamitorishima, Japan	mnm_19C0	153.97	24.3	8	O7
South China Sea	scsn06_01D1	107	6	15	O7
South China Sea	scsn09_01D1	109	9	15	O7
South China Sea	scsn12_01D1	111	12	15	O7
South China Sea	scsn15_01D1	113	15	15	O7
South China Sea	scsn18_01D1	115	18	15	O7
South China Sea	scsn21_01D1	117	21	15	O7
Yonagunijima, Japan	yon_19C0	123.02	24.47	30	O7
Terceira Island, Azores, Portugal	azr_01D0	-27.38	38.77	40	O8
Bermuda Institute of Ocean Sciences	bme_01D0	-64.65	32.37	30	O8
St. Croix, Virgin Islands	avi_01D0	-64.75	17.75	3	O9
Izana Observatory, Spain	izo_01D0	-16.48	28.3	2360	O9
Key Biscayne, Florida	key_01D0	-80.2	25.67	3	O9
Ragged Point, Barbados	rpb_01D0	-59.43	13.17	45	O9
Ascension Island, United Kingdom	asc_01D0	-14.42	-7.92	54	O10
Cape Point, South Africa	cpt_36C0	18.49	-34.35	260	O11
Cape Rama, India	cri_02D0	73.83	15.08	60	O12
Darwin, Northern Territory, Australia	daa_02D0	130.57	-12.42	3	O13
Seychelles Bureau of Standards	sey_01D0	55.17	-4.67	3	O13
Tromelin Island, France	trm_11D0	54.52	-15.88	20	O13

Table A1. Continued.

Station_name	Abbreviation	Longitude	Latitude	Height	Group
Alert, Nunavut, Canada	alt_01D0	-62.52	82.45	210	O14
Iceland	ice_01D0	-20.29	63.34	118	O14
Mould Bay, Nunavut, Canada	mbc_01D0	-119.35	76.25	58	O14
Shetland Islands, Scotland	sis_02D0	-1.17	60.17	30	O14
Ocean Station M, Norway	stm_01D0	2	66	5	O14
Westerland, Germany	wes_23C0	8	55	8	O14
Zeppelin Station, Norway	zep_01D0	11.88	78.9	475	O14
Cape Grim, Tasmania, Australia	aia005_02D2	144.3	-40.53	500	O15
Crozet Islands, France	crz_01D0	51.85	-46.45	120	O15
Casey, Antarctica, Australia	cya_02D0	110.52	-66.28	2	O15
Halley Station, Antarctica	hba_01D0	-26.5	-75.58	30	O15
Jubany Station, Argentina	jbn_29C0	-58.82	-62.23	15	O15
Mawson Station, Antarctica	maa_02D0	62.87	-67.62	32	O15
Macquarie Island, Australia	mqa_02D0	158.97	-54.48	12	O15
Palmer Station, Antarctica	psa_01D0	-64	-64.92	10	O15
Syowa Station, Antarctica	syo_01D0	39.58	-69	11	O15
Argyle, Maine, United States	amt012_01C3	-68.68	45.03	62	L1
Barrow, Alaska	brw_01C0	-156.6	71.32	11	L1
Candle Lake, Canada	cdl030_06C3	-105.12	53.99	630	L1
Cape Meares, Oregon	cmo_01D0	-123.97	45.48	30	L1
Dahlen, North Dakota	dnd010_01P2	-97.77	48.38	1000	L1
Egbert, Ontario, Canada	egb_06C0	-79.78	44.23	226	L1
Fraserdale, Canada	fsd040_06C0	-81.57	49.88	250	L1
Harvard Forest, Massachusetts	hfm005_01P2	-72.17	42.54	500	L1
Park Falls, Wisconsin	lef010_01P2	-90.27	45.93	1000	L1
Lac La Biche, Canada	llb010_06C3	-112.45	54.95	550	L1
Worcester, Massachusetts	nha005_01P2	-70.63	42.95	500	L1
Olympic Peninsula, Washington	opw_01D0	-124.42	48.25	488	L1
Poker Flat, Alaska	pfa015_01P2	-147.29	65.07	1500	L1
Boulder Atmospheric Observatory, Colorado	bao022_01C3	-105.01	40.05	1606	L2
Beaver Crossing, Nebraska	bne010_01P2	-97.18	40.8	1000	L2
Hidden Peak, Utah	hdpda_03C0	-111.65	40.56	3369	L2
Homer, Illinois	hil010_01P2	-87.91	40.07	1000	L2
Grifton, North Carolina	itn051_01C3	-77.38	35.35	60	L2
Southern Great Plains	sgp374_01D0	-97.48	36.62	688	L2
Storm Peak Laboratory	splda_03C0	-106.73	40.45	3219	L2
West Branch, Iowa	wbi010_01P2	-91.35	41.72	1000	L2
Moody, Texas	wkt030_01C3	-97.62	31.32	281	L2
Sary Taukum, Kazakhstan	kzd_01D0	75.57	44.45	412	L7
Plateau Assy, Kazakhstan	kzm_01D0	77.88	43.25	2519	L7
Ulaan Uul, Mongolia	uum_01D0	111.1	44.45	914	L7
Ryori BAPMon Station, Japan	ryo_19C0	141.83	39.03	260	L8
Waliguan, China	wlg_01D0	100.9	36.29	3810	L8
Baltic Sea, Poland	bal_01D1	17.22	55.35	28	L11
Black Sea, Constanta, Romania	bsc_01D0	28.68	44.17	3	L11
Cimone Station, Italy	cmn_17C0	10.7	44.18	2165	L11
Hohenpeißenberg, Germany	hpb_01D0	11.01	47.8	985	L11
Mace Head, Ireland	mhd_01D0	-9.9	53.33	25	L11
Orleans, France	ori005_11D2	2.5	47.8	500	L11
Pallas-Sammaltunturi, Finland	pal_01D0	24.12	67.97	560	L11
Pic Du Midi, France	pdm_11D0	0.13	42.93	2877	L11
Schauinsland, Germany	sch_23C0	8	48	1205	L11

*Acknowledgements.* This work was supported by grants CAS-XDA05100501. The two anonymous reviewers are gratefully acknowledged for their helpful comments and suggestions.

Edited by: M. Kopacz

## References

- Baker, D. F., Law, R. M., Gurney, K. R., Rayner, P., Peylin, P., Denning, A. S., Bousquet, P., Bruhwiler, L., Chen, Y. H., Ciais, P., Fung, I. Y., Heimann, M., John, J., Maki, T., Maksyutov, S., Masarie, K., Prather, M., Pak, B., Taguchi, S., and Zhu, Z.: TransCom 3 inversion intercomparison: Impact of transport model errors on the interannual variability of regional CO<sub>2</sub> fluxes, 1988–2003. *Global Biogeochem. Cy.*, 20, GB1002, doi:10.1029/2004gb002439, 2006.
- Baker, T. R., Phillips, O. L., Malhi, Y., Almeida, S., Arroyo, L., Di Fiore, A., Erwin, T., Higuchi, N., Killeen, T. J., and Laurance, S. G.: Increasing biomass in Amazonian forest plots. *Philos. T. Roy. Soc. London*, 359, 353–365, doi:10.1098/rstb.2003.1422, 2004.
- Bishop, J. K. B. and Rossow, W. B.: Spatial and temporal variability of global surface solar irradiance. *J. Geophys. Res.*, 96, 16839–16858, 1991.
- Bousquet, P.: Regional Changes in Carbon Dioxide Fluxes of Land and Oceans Since 1980. *Science*, 290, 1342–1346, doi:10.1126/science.290.5495.1342, 2000.
- Bousquet, P., Ciais, P., Peylin, P., Ramonet, M., and Monfray, P.: Inverse modeling of annual atmospheric CO<sub>2</sub> sources and sinks 1. Method and control inversion. *J. Geophys. Res.*, 104, 26161–26126, 1999.
- Ciais, P., Rayner, P., Chevallier, F., Bousquet, P., Logan, M., Peylin, P., and Ramonet, M.: Atmospheric inversions for estimating CO<sub>2</sub> fluxes: Methods and perspectives. *Climatic Change*, 103, 69–92, 2010.
- Chevallier, F., Ciais, P., Conway, T., Aalto, T., Anderson, B., Bousquet, P., Brunke, E., Ciattaglia, L., Esaki, Y., and Fröhlich, M.: CO<sub>2</sub> surface fluxes at grid point scale estimated from a global 21 year reanalysis of atmospheric measurements. *J. Geophys. Res.*, 115, D21307, doi:10.1029/2010JD013887, 2010.
- Conway, T., Tans, P., Waterman, L., Thoning, K., Kitzis, D., Masarie, K., and Zhang, N.: Evidence for interannual variability of the carbon cycle from the NOAA/CMDL global air sampling network. *J. Geophys. Res.*, 99, 831–822, 1994.
- DeFries, R. S. and Townshend, J. R. G.: NDVI-derived land cover classifications at a global scale. *Int. J. Remote Sens.*, 15, 3567–3586, 1994.
- Enting, I. G.: Inverse problems in atmospheric constituent transport. Cambridge Univ. Pr, 2002.
- Feng, L., Palmer, P. I., Yang, Y., Yantosca, R. M., Kawa, S. R., Paris, J.-D., Matsueda, H., and Machida, T.: Evaluating a 3-D transport model of atmospheric CO<sub>2</sub> using ground-based, aircraft, and space-borne data. *Atmos. Chem. Phys.*, 11, 2789–2803, doi:10.5194/acp-11-2789-2011, 2011.
- GLOBALVIEW-CO<sub>2</sub>: Cooperative Atmospheric Data Integration Project – Carbon Dioxide., NOAA ESRL, Boulder, Colorado, 2010.
- Gurney, K. R.: Transcom 3 inversion intercomparison: Model mean results for the estimation of seasonal carbon sources and sinks. *Global Biogeochem. Cy.*, 18, GB1010, doi:10.1029/2003gb002111, 2004.
- Gurney, K. R., Law, R. M., Denning, A. S., Rayner, P. J., Baker, D., Bousquet, P., Bruhwiler, L., Chen, Y. H., Ciais, P., and Fan, S.: Towards robust regional estimates of CO<sub>2</sub> sources and sinks using atmospheric transport models. *Nature*, 415, 626–630, 2002.
- Hansen, J., Ruedy, R., Glascoe, J., and Sato, M.: GISS analysis of surface temperature change. *J. Geophys. Res.*, 104, 30997–31022, 1999.
- Kaminski, T., Heimann, M., and Giering, R.: A global scale inversion of the transport of CO<sub>2</sub> based on a matrix representation of an atmospheric transport model derived by its adjoint. *NATO Challenges of Modern Society*, 22, 247–258, 1998.
- Metzl, N., Brunet, C., Jabaudjan, A., Poisson, A., and Schauer, B.: Summer and winter air–sea CO<sub>2</sub> fluxes in the Southern Ocean. *Deep Sea Res. Pt. I*, 53, 1548–1563, doi:10.1016/j.dsr.2006.07.006, 2006.
- Mitchell, T. D. and Jones, P. D.: An improved method of constructing a database of monthly climate observations and associated high-resolution grids. *Int. J. Climatol.*, 25, 693–712, 2005.
- Nassar, R., Jones, D. B. A., Suntharalingam, P., Chen, J. M., Andres, R. J., Wecht, K. J., Yantosca, R. M., Kulawik, S. S., Bowman, K. W., Worden, J. R., Machida, T., and Matsueda, H.: Modeling global atmospheric CO<sub>2</sub> with improved emission inventories and CO<sub>2</sub> production from the oxidation of other carbon species. *Geosci. Model Dev.*, 3, 689–716, doi:10.5194/gmd-3-689-2010, 2010.
- Nassar, R., Jones, D. B. A., Kulawik, S. S., Worden, J. R., Bowman, K. W., Andres, R. J., Suntharalingam, P., Chen, J. M., Breninkmeijer, C. A. M., Schuck, T. J., Conway, T. J., and Worthy, D. E.: Inverse modeling of CO<sub>2</sub> sources and sinks using satellite observations of CO<sub>2</sub> from TES and surface flask measurements. *Atmos. Chem. Phys.*, 11, 6029–6047, doi:10.5194/acp-11-6029-2011, 2011.
- New, M., Hulme, M., and Jones, P.: Representing twentieth century space–time climate variability. Part I: development of a 1961–90 mean monthly terrestrial climatology. *J. Climate*, 12, 829–856, 1999.
- Olsen, S. C.: Differences between surface and column atmospheric CO<sub>2</sub> and implications for carbon cycle research. *J. Geophys. Res.*, 109, D02301, doi:10.1029/2003jd003968, 2004.
- Peylin, P., Baker, D., Sarmiento, J., Ciais, P., and Bousquet, P.: Influence of transport uncertainty on annual mean and seasonal inversions of atmospheric CO<sub>2</sub> data. *J. Geophys. Res.*, 107, 4385, doi:10.1029/2001JD000857, 2002.
- Piao, S., Ciais, P., Friedlingstein, P., Peylin, P., Reichstein, M., Luysaert, S., Margolis, H., Fang, J., Barr, A., Chen, A., Grelle, A., Hollinger, D. Y., Laurila, T., Lindroth, A., Richardson, A. D., and Vesala, T.: Net carbon dioxide losses of northern ecosystems in response to autumn warming. *Nature*, 451, 49–52, doi:10.1038/nature06444, 2008.
- Raich, J. W. and Potter, C. S.: Global patterns of carbon dioxide emissions from soils. *Global Biogeochem. Cy.*, 9, 23–36, 1995.
- Randerson, J. T., Thompson, M. V., Conway, T. J., Fung, I. Y., and Field, C. B.: The contribution of terrestrial sources and sinks to trends in the seasonal cycle of atmospheric carbon dioxide. *Global Biogeochem. Cy.*, 11, 535–560, 1997.
- Rödenbeck, C., Conway, T. J., and Langenfelds, R. L.: The effect of systematic measurement errors on atmospheric CO<sub>2</sub> inver-

- sions: a quantitative assessment, *Atmos. Chem. Phys.*, 6, 149–161, doi:10.5194/acp-6-149-2006, 2006.
- Shea, D. J.: Climatological atlas: 1950–1979, Technical Note NCAR TN-269+STR, Nat. Cent. for Atmos. Res., Boulder, Colorado, 1986.
- Sitch, S., Huntingford, C., Gedney, N., Levy, P., Lomas, M., Piao, S., Betts, R., Ciais, P., Cox, P., and Friedlingstein, P.: Evaluation of the terrestrial carbon cycle, future plant geography and climate-carbon cycle feedbacks using five Dynamic Global Vegetation Models (DGVMs), *Glob. Change Biol.*, 14, 2015–2039, 2008.
- Stephens, B. B., Gurney, K. R., Tans, P. P., Sweeney, C., Peters, W., Bruhwiler, L., Ciais, P., Ramonet, M., Bousquet, P., and Nakazawa, T.: Weak northern and strong tropical land carbon uptake from vertical profiles of atmospheric CO<sub>2</sub>, *Science*, 316, 1732, doi:10.1126/science.1137004, 2007.
- Suntharalingam, P.: Improved quantification of Chinese carbon fluxes using CO<sub>2</sub>/CO correlations in Asian outflow, *J. Geophys. Res.*, 109, D18S18, doi:10.1029/2003jd004362, 2004.
- Suntharalingam, P.: Influence of reduced carbon emissions and oxidation on the distribution of atmospheric CO<sub>2</sub>: Implications for inversion analyses, *Global Biogeochem. Cy.*, 19, GB4003, doi:10.1029/2005gb002466, 2005.
- Tans, P. P., Conway, T. J., and Nakazawa, T.: Latitudinal distribution of the sources and sinks of atmospheric carbon dioxide derived from surface observations and an atmospheric transport model, *J. Geophys. Res.*, 94, 5151–5172, 1989.
- Tans, P. P., Fung, I. Y., and Takahashi, T.: Observational constraints on the global atmospheric CO<sub>2</sub> budget, *Science*, 247, 1431–1438, 1990.
- Xie, P. and Arkin, P. A.: Analyses of global monthly precipitation using gauge observations, satellite estimates, and numerical model predictions, *J. Climate*, 9, 840–858, 1996.
- Zeng, N.: Glacial-interglacial atmospheric CO<sub>2</sub> change – The glacial burial hypothesis, *Adv. Atmos. Sci.*, 20, 677–693, 2003.
- Zeng, N., Mariotti, A., and Wetzel, P.: Terrestrial mechanisms of interannual CO<sub>2</sub> variability, *Global Biogeochem. Cy.*, 19, GB1016, doi:10.1029/2004GB002273, 2005.
- Zobler, L. A.: World soil file for global climate modeling, NASA Tech. Memo., 87802, 32 pp., 1986.